

AHAP: Reconstructing Arbitrary Humans from Arbitrary Perspectives with Geometric Priors

Xiaozhen Qiao^{1,2*} Wenjia Wang^{3*} Zhiyuan Zhao¹ Jiacheng Sun⁴ Ping Luo³
Hongyuan Zhang^{1,3†} Xuelong Li^{1†}

Project Page: [AHAP](#) * Equal Contribution † Corresponding Authors

Abstract

Reconstructing 3D humans from images captured at multiple perspectives typically requires pre-calibration, like using checkerboards or MVS algorithms, which limits scalability and applicability in diverse real-world scenarios. In this work, we present **AHAP** (Reconstructing Arbitrary Humans from Arbitrary Perspectives), a feed-forward framework for reconstructing arbitrary humans from arbitrary camera perspectives without requiring camera calibration. Our core lies in the effective fusion of multi-view geometry to assist human association, reconstruction and localization. Specifically, we use a Cross-View Identity Association module through learnable person queries and soft assignment, supervised by contrastive learning to resolve cross-view human identity association. A Human Head fuses cross-view features and scene context for SMPL prediction, guided by cross-view reprojection losses to enforce body pose consistency. Additionally, multi-view geometry eliminates the depth ambiguity inherent in monocular methods, providing more precise 3D human localization through multi-view triangulation. Experiments on EgoHumans and EgoExo4D demonstrate that AHAP achieves competitive performance on both world-space human reconstruction and camera pose estimation, while being 180× faster than optimization-based approaches.

1. Introduction

Efficient and accurate reconstruction of both scene geometry (Wang et al., 2024b; 2025a; Lin et al., 2025), and human bodies (Ge et al., 2024; Wang et al., 2023b) in a shared

¹Institute of Artificial Intelligence (TeleAI), China Telecom, P. R. China. ²University of Science and Technology of China. ³University of Hong Kong. ⁴Huawei Technologies Co., Ltd..

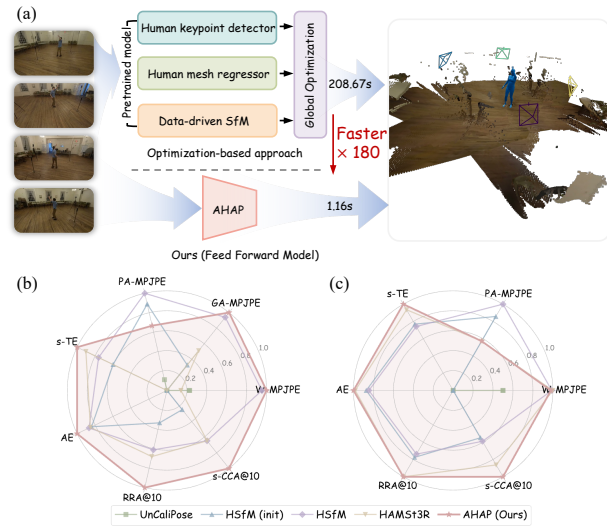


Figure 1. (a) AHAP achieves 180× speedup over optimization-based HSfM (Müller et al., 2025) while maintaining competitive accuracy. (b) Results on EgoHumans. (c) Results on EgoExo4D.

world coordinate system is crucial for Embodied AI (Wang et al., 2025b; Li et al., 2026; Salzmänn et al., 2023; Fu et al., 2026; Huang et al., 2025), Virtual Reality, and Motion Analysis (Dao et al., 2025; Chen et al., 2025a). Multi-view observations (Zhu et al., 2025) offer complementary visibility that alleviates occlusion and depth ambiguity while providing essential geometric constraints for aligning humans and scenes. Existing multi-view human-scene reconstruction methods (Müller et al., 2025; Rojas et al., 2025) typically rely on iterative test-time optimization to refine cross-view consistency among human meshes, cameras, and geometry. While accurate, these paradigms involve expensive optimization cycles and repeated reprojections, leading to high latency and limited scalability for real-time applications. This naturally raises the question:

Can consistent 3D reconstruction of arbitrary humans and scenes be achieved in a purely feed-forward manner from arbitrary perspectives?

Achieving this in uncalibrated, multi-person scenarios is particularly challenging. The same individual can exhibit

Table 1. **Comparison of method capabilities.** AHAP is the first feed-forward method to jointly reconstruct scene geometry and cameras from uncalibrated arbitrary-view images.

Method	Feed-fwd	Multi-Person	Camera	Scene
Multi-HMR (Baradel et al., 2024)	✓	✓	✗	✗
SLAHMR (Ye et al., 2023a)	✗	✓	✓	✗
UnCaliPose (Xu & Kitani, 2022)	✗	✓	✓	✗
HSfM (Müller et al., 2025)	✗	✓	✓	✓
HAMS3R (Rojas et al., 2025)	✗	✓	✓	✓
AHAP (Ours)	✓	✓	✓	✓

drastic appearance changes and severe occlusions across viewpoints, while the co-occurrence of multiple people necessitates reliable cross-view identity association for correct fusion. Simultaneously, predictions from all viewpoints must be registered into a unified world coordinate system, requiring robust cross-view geometric reasoning and joint camera recovery without pre-calibrated extrinsics. Beyond the computational burden of optimization-based methods, current feed-forward alternatives fall short: single-view methods process viewpoints independently, failing to leverage cross-view complementarity (Baradel et al., 2024; Wang et al., 2025c), while multi-view feed-forward methods either require pre-calibrated cameras or resort to post-hoc optimization for SMPL fitting, precluding end-to-end geometric supervision during training (Müller et al., 2025; Rojas et al., 2025). Furthermore, many approaches remain restricted to single-person settings (Li et al., 2024). Consequently, the joint recovery of multiple humans, scene geometry, and camera poses via a purely feed-forward pass from uncalibrated arbitrary-view inputs remains an open problem (Table 1).

To address these limitations, we propose **AHAP** (Reconstructing **A**rbitrary **H**umans from **A**rbitrary **P**erspectives), a unified feed-forward framework for multi-person human-scene reconstruction from uncalibrated, arbitrary-view inputs. Our core insight lies in the effective fusion of multi-view geometry to jointly solve human association, reconstruction, and localization in a single forward pass. Specifically, we introduce a Cross-View Identity Association module that ensures robust identity consistency across disparate viewpoints via learnable person queries and a soft assignment mechanism. This learnable association is supervised by contrastive learning and leverages discriminative semantic features to resolve the challenges of appearance changes and severe occlusions, which effectively eliminates the necessity of traditional 2D tracking methods like (Ye et al., 2023b; Rajasegaran et al., 2022). Guided by these associations, a specialized Human Head decodes aggregated multi-view features alongside dense scene context to directly regress SMPL parameters (Loper et al., 2023). This joint reasoning significantly improves pose accuracy by leveraging complementary visibility to alleviate self-occlusions and depth ambiguities inherent in monocular methods (Baradel et al., 2024; Khirodkar et al., 2023). The reconstruction is further regularized by a cross-view reprojection loss to enforce body pose consistency across all viewpoints. Finally,

to overcome the imprecise 3D localization of single-view estimation, AHAP leverages the precise 2D localization from our human branch and the 3D geometric reasoning of the scene branch to apply multi-view triangulation at inference.

Experiments on EgoHumans (Khirodkar et al., 2023) and EgoExo4D (Grauman et al., 2024) demonstrate competitive performance on both human reconstruction and camera pose estimation, while achieving 180× speedup over optimization-based methods (Figure 1). Our main contributions are:

- We present AHAP, the first **feed-forward** framework for the joint reconstruction of arbitrary humans, scene geometry, and camera poses from uncalibrated arbitrary perspectives.
- We propose a cross-view **identity association** module that uses learnable queries and soft assignment to establish correspondences across viewpoints. This approach is supervised through contrastive learning to achieve discriminative matching, eliminating the reliance on visual tracking.
- We design a Human Head that jointly decodes cross-view aggregated features with scene context to predict SMPL parameters, supervised by cross-view reprojection losses for **body pose consistency**.
- We employ scale alignment and multi-view triangulation at inference to **localize human positions** and improve global human-scene alignment in the world coordinate system.

2. Related Works

Multi-View Geometry. Classical Multi-View Geometry methods (Agarwal et al., 2011; Frahm et al., 2010; Liu et al., 2024), such as COLMAP (Schonberger & Frahm, 2016), reconstruct 3D scenes via multi-stage pipelines with feature matching, triangulation, and bundle adjustment. While accurate, their reliance on handcrafted components and iterative optimization limits robustness and scalability. Recent differentiable SfM (Wang et al., 2024a; Lee & Yoo, 2025) enables joint learning of geometry and camera parameters. In parallel, point-map-based approaches directly regress globally aligned 3D structures from sparse views, bypassing explicit optimization (Wang et al., 2024b; Leroy et al., 2024). VGGT (Wang et al., 2025a) unifies camera poses, depth, point maps, and tracks within a feed-forward transformer, while Depth Anything v3 (DA3) (Lin et al., 2025) predicts spatially consistent 3D geometry and camera poses from arbitrary visual inputs via a unified depth-ray representation. Our method extends this paradigm by incorporating human reconstruction in a feed-forward manner, and further

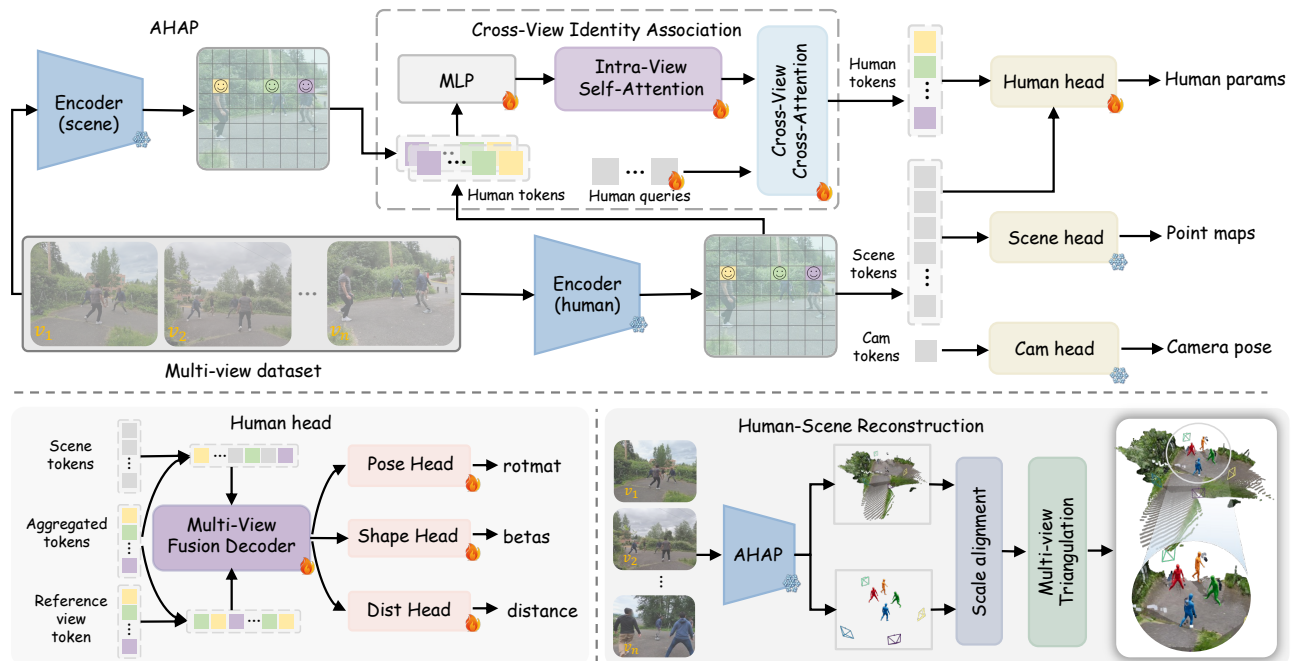


Figure 2. **Overall pipeline of AHAP.** Given multi-view images, the scene encoder (Lin et al., 2025) estimates scene geometry and camera poses, while the human encoder (Baradel et al., 2024) extracts human-centric features. Our cross-view identity association module matches the same person across views via learnable queries. The human head fuses scene tokens, aggregated tokens, and reference view tokens through a multi-view fusion decoder to predict SMPL parameters. Finally, we align humans and scene point clouds via scale alignment and multi-view triangulation for precise human localization.

improves scene geometry prediction through human-scene joint reasoning.

Feed-Forward Human Mesh Reconstruction. Feed-Forward Human mesh reconstruction aims to recover parametric body models, such as SMPL (Loper et al., 2023) and SMPL-X (Pavlakos et al., 2019). Early methods focus on single-person monocular reconstruction by regressing body parameters from cropped images, with later approaches improving robustness through stronger backbones and large-scale supervision (Wang et al., 2023b). One-stage frameworks such as Multi-HMR (Baradel et al., 2024) extend to multi-person monocular reconstruction, while PromptHMR (Wang et al., 2025c) enables flexible control via spatial and semantic prompts on full images. Beyond monocular input, multi-view methods such as U-HMR (Li et al., 2024) exploit geometric constraints to resolve depth ambiguities, but remain limited to single-person scenarios. Multi-person multi-view reconstruction is still underexplored due to challenges in cross-view correspondence and inter-person occlusion, which motivates our feed-forward approach for arbitrary-human arbitrary-view reconstruction.

Human-Scene Reconstruction. Joint reconstruction of humans and scenes has attracted increasing attention. HSfM (Müller et al., 2025) integrates human body constraints into a traditional Structure from Motion (SfM) pipeline to achieve metric-scale recovery, yet its reliance on

iterative optimization limits scalability. HAMSt3R (Rojas et al., 2025) extends pointmap-based representation with human-specific heads for instance and DensePose prediction, though its post-hoc SMPL fitting remains a bottleneck. Human3R (Chen et al., 2025b) achieves unified reconstruction from monocular video, it is constrained by single-view inputs. Earlier uncalibrated multi-view methods like UniCaliPose (Xu & Kitani, 2022) focus on pose estimation via cross-view matching but lack dense scene context. Our work operates in multi-view settings, enabling a unified feed-forward reconstruction of arbitrary humans and scenes from arbitrary perspectives.

3. Method

Given S multi-view images $I_{i=1}^S$ of the same scene with human presence, our goal is to jointly reconstruct 3D human meshes and scene geometry with consistent identities across viewpoints in a feed-forward manner. Unlike existing paradigms that either process views independently (Baradel et al., 2024; Wang et al., 2025c) or rely on expensive iterative optimization (Xu & Kitani, 2022; Yin et al., 2025; Müller et al., 2025), AHAP achieves this in a single forward pass.

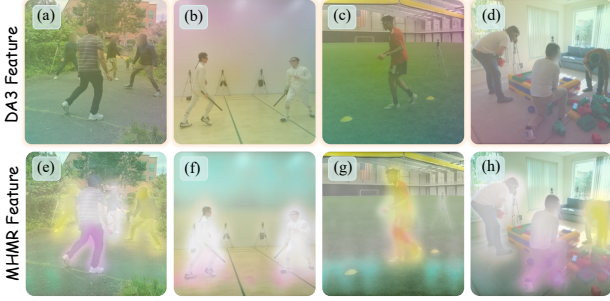


Figure 3. **PCA visualization of feature distributions.** (a-d) Scene encoder (Lin et al., 2025) features; (e-h) Human encoder (Baradel et al., 2024) features. Human encoder features show stronger semantic clustering aligned with ground truth, while scene encoder provides complementary geometric information.

3.1. Overview

As illustrated in Figure 2, achieving arbitrary-view human-scene reconstruction requires addressing three core challenges: (1) establishing consistent human identity correspondences across uncalibrated views, (2) effectively aggregating multi-view features for accurate human mesh reconstruction, and (3) ensuring geometric consistency between reconstructed humans and the scene. To this end, Section 3.3 introduces a cross-attention-based association module that learns soft assignment across views. Section 3.4 presents the Human Head that fuses aggregated multi-view features with scene context for SMPL prediction. Section 3.5 details our multi-task supervision scheme enforcing cross-view geometric consistency. Finally, Section 3.6 describes metric measurement and metric measurement and inference-time triangulation for global human-scene alignment.

3.2. Visual Feature Encoding

To capture complementary visual information, we leverage two pre-trained backbones. The scene branch utilizes DA3 (Lin et al., 2025) to extract dense geometric features F^{scene} , while the human branch employs a Multi-HMR (Baradel et al., 2024) backbone to extract human-centric semantic features F^{human} alongside a detection head for localization. As shown in Figure 3, human features exhibit strong semantic clustering, whereas scene encoder provides critical geometric context. At each detected human location (h, w) in the human feature map, we map to the corresponding scene location (h', w') via resolution alignment, then fuse tokens through a two-layer MLP

$$\mathbf{z} = \mathcal{M}_{\text{fuse}} \left([F_{h,w}^{\text{human}}; F_{h',w'}^{\text{scene}}] \right) \in \mathbb{R}^D, \quad (1)$$

where $D = 1024$. These fused tokens integrate discriminative appearance cues with scene-aware geometric information, serving as the input for our cross-view identity association module.

3.3. Cross-View Identity Association

The core challenge in multi-view human reconstruction is establishing human identity correspondences across views without explicit 3D supervision. We propose a soft-assignment based association module that learns to match detections belonging to the same person.

Before cross-view association, we first enhance each detection representation through intra-view self-attention. For detections $\{z_1, \dots, z_{N_v}\}$ in view v , multi-head self-attention is applied to enable awareness of other people in the same view

$$\tilde{z}_j = \text{LN} \left(z_j + \text{SA} \left(z_j, \{z_k\}_{k=1}^{N_v} \right) \right), \quad (2)$$

To establish cross-view correspondences, learnable person queries $Q \in \mathbb{R}^{P \times D}$ are introduced, where $P = 36$ is the maximum number of persons and $D = 1024$. Given all enhanced detection tokens $\{\tilde{z}_n\}_{n=1}^N$ from all views, we compute soft assignment through multi-head cross-attention

$$A = \frac{1}{H} \sum_{h=1}^H \text{softmax} \left(\frac{QW_h^Q (KW_h^K)^\top}{\sqrt{D/H}} \right) \in \mathbb{R}^{P \times N}, \quad (3)$$

where $K = [\tilde{z}_1, \dots, \tilde{z}_N]^\top$ are the detection tokens serving as keys and values, and $H = 8$ is the number of attention heads. Each row $A_{p,:}$ represents the probability distribution of person query p attending to all detections, effectively learning which detections belong to the same individual. The final assignment is $\text{person}(n) = \arg \max_p A_{p,n}$.

For each person p , we aggregate features from all associated detections via weighted sum

$$f_p^{\text{agg}} = \text{LN} (A_{p,:} \cdot K) \in \mathbb{R}^D. \quad (4)$$

This weighted sum naturally handles occlusions and varying numbers of viewpoints per person by prioritizing high-confidence features.

3.4. Arbitrary View Human Head

To achieve cross-view consistent SMPL recovery, the Human Head incorporates aggregated multi-view information into a transformer-based decoder. While prediction is performed within a reference view, typically the one with the highest detection density, the process is guided by the global representation f_p^{agg} .

We construct context features by combining human features $F^{\text{human}} \in \mathbb{R}^{H \times W \times 1024}$, projected DA3 features $\text{Proj}(F^{\text{scene}}) \in \mathbb{R}^{H \times W \times 1024}$, and Fourier camera ray embeddings $E^{\text{cam}} \in \mathbb{R}^{H \times W \times 99}$ (Mildenhall et al., 2021). The aggregated multi-view feature f_p^{agg} is then projected and added to the context

$$\tilde{C} = C + \sigma(\alpha) \cdot \text{Broadcast} \left(\text{Proj}_{\text{kv}}(f_p^{\text{agg}}) \right), \quad (5)$$

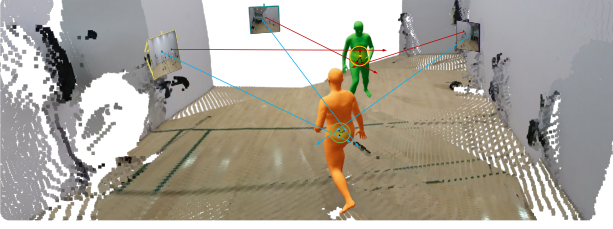


Figure 4. Multi-view triangulation for human position refinement. For persons visible in multiple views, we refine their 3D positions using DLT triangulation based on 2D pelvis observations and estimated camera poses, improving human-scene alignment.

where $\sigma(\alpha)$ is a learnable scale initialized near zero for training stability. Additionally, the aggregated feature is projected as an auxiliary query token $\mathbf{q}_{mv} = \text{Proj}_q(\mathbf{f}_p^{\text{agg}})$.

The context feature at the detection location is augmented with mean SMPL parameters to form the primary query $\mathbf{q}_{\text{det}} = [z; \bar{\theta}; \bar{\beta}; \bar{c}]$. Both queries are processed together through cross-attention (Jaegle et al., 2021; Dosovitskiy, 2020) with the multi-view enhanced context:

$$\mathbf{q}_{\text{final}} = \text{CA} \left([\mathbf{q}_{\text{det}}; \mathbf{q}_{mv}], \tilde{\mathbf{C}}, \tilde{\mathbf{C}} \right). \quad (6)$$

The final prediction is

$$\boldsymbol{\theta} = \bar{\boldsymbol{\theta}} + \mathcal{M}_{\text{pose}}(\mathbf{q}_{\text{final}}), \quad (7)$$

$$\boldsymbol{\beta} = \bar{\boldsymbol{\beta}} + \mathcal{M}_{\text{shape}}(\mathbf{q}_{\text{final}}), \quad (8)$$

$$\mathbf{d} = \mathcal{M}_{\text{cam}}(\mathbf{q}_{\text{final}}), \quad (9)$$

where $\boldsymbol{\theta}$ denotes pose parameters, $\boldsymbol{\beta}$ denotes shape parameters, and \mathbf{d} denotes distance (Kanazawa et al., 2018). Unlike post-hoc fitting methods that rely on iterative refinement, this feed-forward head directly leverages multi-view complementarity to resolve depth and pose ambiguities.

3.5. Training Details

To supervise the association module and enforce geometric consistency, three complementary loss functions are designed.

Soft Assignment Loss. We directly supervise the attention weights in Equation (3) using ground-truth correspondences. Given the target assignment matrix \mathbf{A}^* , predicted identities are aligned with ground-truth labels via Hungarian matching, followed by the computation of a cross-entropy loss:

$$\mathcal{L}_{\text{assign}} = -\frac{1}{P^*} \sum_{p=1}^{P^*} \sum_{n=1}^N \tilde{\mathbf{A}}_{p,n}^* \log \mathbf{A}_{\pi(p),n}, \quad (10)$$

where π is the optimal matching and $\tilde{\mathbf{A}}^*$ is row-normalized.

Contrastive Loss. To learn discriminative features for association, we apply InfoNCE (Oord et al., 2018) where

detections of the same person across views form positive pairs

$$\mathcal{L}_{\text{contra}} = -\frac{1}{|\mathcal{P}|} \sum_{(i,j) \in \mathcal{P}} \log \frac{\exp(\mathbf{h}_i \cdot \mathbf{h}_j^+ / \tau)}{\sum_k \exp(\mathbf{h}_i \cdot \mathbf{h}_k / \tau)}, \quad (11)$$

where $\tau = 0.07$ is the temperature and $\mathbf{h} = \text{Proj}(\tilde{\mathbf{z}})$ are L2-normalized projections of the enhanced human tokens.

Cross-View Reprojection Loss. To enforce geometric consistency, we transform predictions from the reference view to other views using camera extrinsics ($\mathbf{J}_{\text{world}} = \mathbf{C}2\mathbf{W}^{\text{ref}} \cdot \mathbf{J}_{\text{cam}}^{\text{ref}}$, then $\mathbf{J}_{\text{cam}}^v = \mathbf{W}2\mathbf{C}^v \cdot \mathbf{J}_{\text{world}}$) and compare with GT:

$$\mathcal{L}_{\text{reproj}} = \frac{1}{|\mathcal{V}|} \sum_{v \in \mathcal{V}} \left(\|\mathbf{J}_{\text{rel}}^v - \hat{\mathbf{J}}_{\text{rel}}^v\|_1 + \lambda \|\Pi(\mathbf{J}^v) - \hat{\mathbf{J}}_{2d}^v\|_1 \right), \quad (12)$$

where \mathbf{J}_{rel} denotes root-relative 3D joints and $\Pi(\cdot)$ is perspective projection.

The complete training objective is

$$\mathcal{L} = \mathcal{L}_{\text{SMPL}} + \lambda_1 \mathcal{L}_{\text{assign}} + \lambda_2 \mathcal{L}_{\text{contra}} + \lambda_3 \mathcal{L}_{\text{reproj}}, \quad (13)$$

where $\mathcal{L}_{\text{SMPL}}$ is the standard SMPL supervision loss (details in supplementary material).

Two-Stage Training Strategy. We adopt a two-stage curriculum: first training on BEDLAM (Black et al., 2023) temporal sequences. Consecutive frames serve as pseudo multi-view inputs with minimal appearance variation, allowing the association module to learn robust identity matching in a simplified setting. Then fine-tuning on EgoHumans (Khironkar et al., 2023) multi-view data. This stage enables the model to generalize to real cross-view scenarios characterized by severe occlusions and drastic appearance changes.

3.6. Human-Scene Reconstruction

During inference, we utilize multi-view geometry to refine human positions and improve the overall human-scene alignment. The camera poses are estimated by the scene branch, which predicts camera-to-world transforms $\{\mathbf{T}_i^{c2w}\}$ relative to a reference view.

Since SMPL predictions and scene depth may have inconsistent scales, we first compute a global scale factor. For each detected human, we sample the scene depth at the pelvis 2D location using a local window and take the median, then compare with the predicted pelvis depth

$$s = \text{median} \left(\frac{z_i^{\text{scene}}}{z_i^{\text{human}}} \right)_{i=1}^N, \quad (14)$$

where N is the number of humans with valid depth pairs. This global scale is applied to all human meshes to ensure consistent sizing across the scene.

Table 2. **Human-centric evaluation metrics** on EgoHumans and EgoExo4D. AHAP achieves competitive W-MPJPE (0.88m) and GA-MPJPE (0.18m) on EgoHumans, outperforming optimization-based HSfM by 15%. While HSfM attains lower PA-MPJPE through iterative refinement, our feed-forward approach remains competitive (0.08m vs. 0.05m) without test-time optimization. **Best** and **second best** results are highlighted.

Type	Method	EgoHumans			EgoExo4D	
		W-MPJPE↓	GA-MPJPE↓	PA-MPJPE↓	W-MPJPE↓	PA-MPJPE↓
Single-view	Multi-HMR (Baradel et al., 2024)	7.66	0.99	0.12	2.88	0.07
	UnCaliPose (Xu & Kitani, 2022)	3.51	0.67	0.13	2.90	0.13
Optimization-based	HSfM (init) (Müller et al., 2025)	4.28	0.51	0.06	5.29	0.07
	HSfM (Müller et al., 2025)	1.04	0.21	0.05	0.56	0.06
	HAMSt3R (Rojas et al., 2025)	3.80	0.42	0.14	0.51	0.09
Feed-forward	AHAP (Ours)	0.88	0.18	0.08	0.60	0.09

Table 3. **Camera pose evaluation** on EgoHumans and EgoExo4D. Feed-forward methods achieve superior rotation accuracy: AHAP obtains AE of 1.47° on EgoHumans (vs. HSfM’s 9.35°) with perfect RRA@10 of 1.00. Compared to DA3, AHAP improves rotation accuracy by 35% (AE: 1.47° vs. 2.26°) and scale-aligned translation by 41% (s-TE: 0.16m vs. 0.27m), demonstrating that joint human-scene learning provides mutually beneficial geometric priors. **Best** and **second best** results are highlighted.

Type	Method	EgoHumans						EgoExo4D					
		TE↓	s-TE↓	AE↓	RRA@10↑	CCA@10↑	s-CCA@10↑	TE↓	s-TE↓	AE↓	RRA@10↑	CCA@10↑	s-CCA@10↑
Opt.-based	UnCaliPose (Xu & Kitani, 2022)	2.63	2.63	60.90	0.28	-	0.33	2.43	1.16	65.61	0.19	-	0.24
	HSfM (init) (Müller et al., 2025)	2.37	1.15	11.00	0.52	0.26	0.49	1.27	0.33	9.92	0.81	0.05	0.64
	HSfM (Müller et al., 2025)	2.09	0.75	9.35	0.72	0.32	0.75	0.95	0.36	11.57	0.78	0.07	0.67
	HAMSt3R (Rojas et al., 2025)	2.33	0.40	10.24	0.77	0.06	0.75	0.60	0.15	2.85	0.99	0.42	0.87
FF	DA3 (Lin et al., 2025)	3.89	0.27	2.26	0.99	-	0.86	1.62	0.07	1.80	0.98	0.02	0.96
	AHAP (Ours)	4.54	0.16	1.47	1.00	-	0.98	1.60	0.08	1.74	0.99	0.30	0.97

Table 4. **Efficiency comparison.** Our method achieves 180–250× speedup over HSfM across different numbers of views.

Method	Num. Views			
	1	2	3	4
HSfM (Müller et al., 2025)	-	180.41s	201.85s	208.67s
AHAP (Ours)	0.34s	0.72s (250×)	0.94s (215×)	1.16s (180×)

For individuals visible in ≥ 2 views, we further refine their 3D positions through Direct Linear Transform (DLT) triangulation. Given 2D pelvis observations $\{(u_i, v_i)\}$ and projection matrices $P_i = K_i[R_i|t_i]$ derived from the estimated camera poses, we construct the linear system:

$$\begin{aligned}
 \mathbf{A}\mathbf{X} &= \mathbf{0}, \quad \text{where} \\
 \mathbf{A}_{2i} &= u_i P_i^{(3)} - P_i^{(1)}, \quad \mathbf{A}_{2i+1} = v_i P_i^{(3)} - P_i^{(2)}.
 \end{aligned} \tag{15}$$

The solution is obtained via SVD as $\mathbf{X}^* = \arg \min_{\|\mathbf{X}\|=1} \|\mathbf{A}\mathbf{X}\|$, where \mathbf{A} is constructed from the 2D pelvis projections across views. We further transform the triangulated translation to camera space for 2D overlay. This refinement step is a closed-form geometric solution that maintains high computational efficiency.

4. Experiments

4.1. Datasets and Metrics

AHAP is trained on the training sets of BEDLAM (Black et al., 2023) and EgoHumans (Khirodkar et al., 2023). Generalization is evaluated on the test splits of EgoHumans and EgoExo4D (Grauman et al., 2024). For human mesh recovery,

we report W-MPJPE, GA-MPJPE, and PA-MPJPE to measure 3D joint errors across different alignment levels. Camera pose accuracy is evaluated using TE, s-TE, AE, RRA@10 (Wang et al., 2023a), CCA@10 (Lin et al., 2024), and s-CCA@10 (Müller et al., 2025). These metrics assess both metric-scale and scale-invariant translation and rotation performance. Detailed definitions are provided in the supplementary material.

4.2. Results

AHAP is evaluated against several baseline methods: the monocular Multi-HMR (Baradel et al., 2024), the uncalibrated pose estimator UnCaliPose (Xu & Kitani, 2022), the optimization-based HSfM (Müller et al., 2025), and the hybrid framework HAMSt3R (Rojas et al., 2025). Quantitative comparisons on the EgoHumans and EgoExo4D datasets are summarized in Tables 2 and 3. Across both benchmarks, AHAP achieves competitive performance in world-space human reconstruction and camera pose estimation. Unlike optimization-based HSfM and HAMSt3R, AHAP recovers SMPL parameters and camera extrinsics via a strictly feed-forward inference. This architecture offers a superior balance between reconstruction fidelity and computational efficiency, yielding a 180× speedup over optimization-heavy baselines.

Human Mesh Recovery. As shown in Table 2, AHAP achieves competitive performance on EgoHumans, particularly excelling in world-space metrics (W-MPJPE, GA-

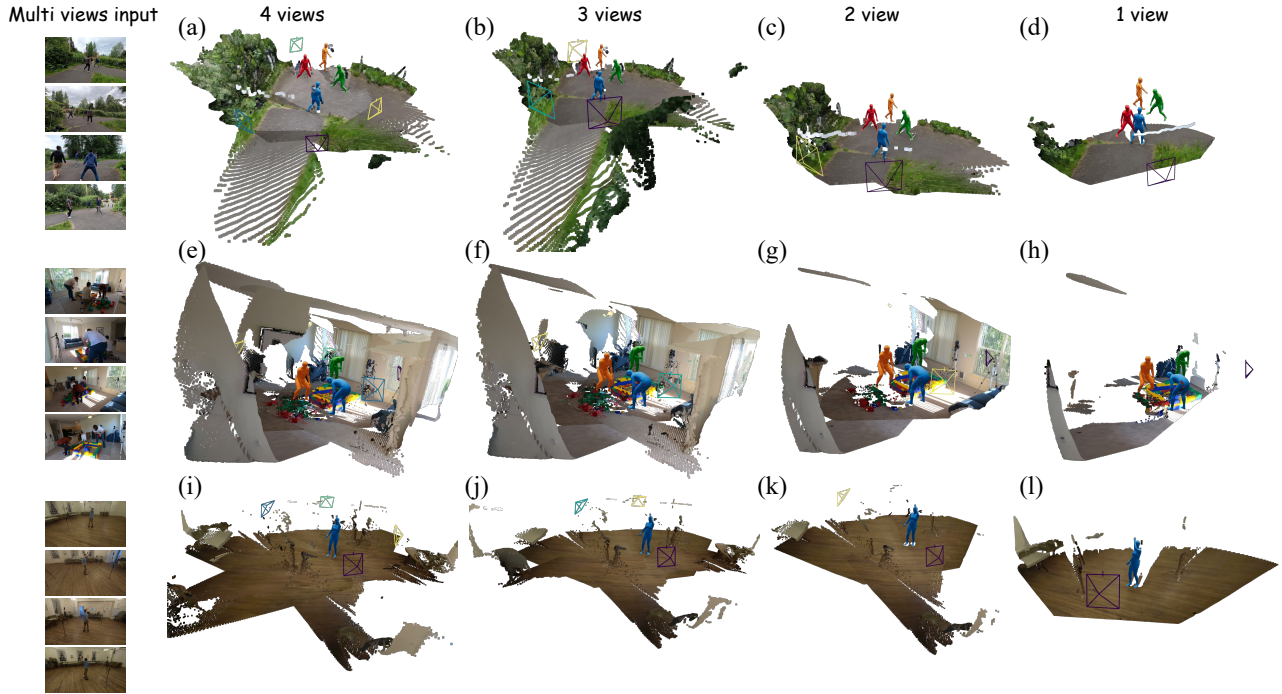


Figure 5. **Qualitative results.** Visualization of human-scene reconstruction on EgoHumans and EgoExo4D. AHAP produces accurate human meshes within reconstructed scenes, maintaining consistent identity association across views.

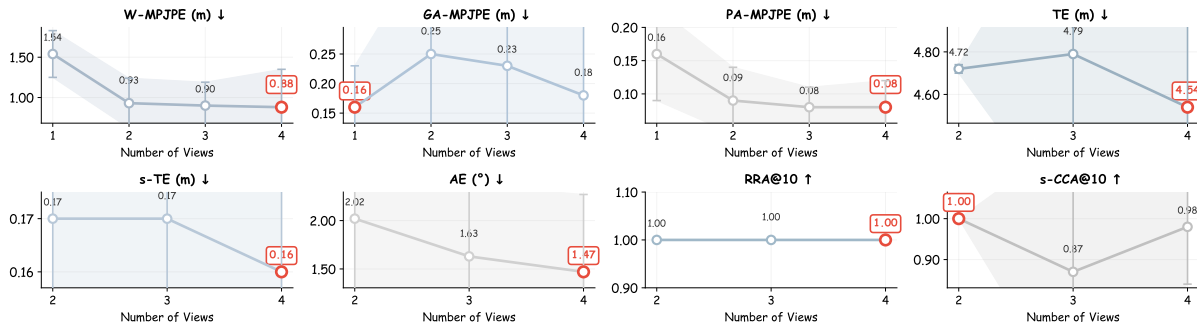


Figure 6. **Ablation study on the number of input views** on EgoHumans. AHAP consistently improves as more views become available. The first additional view provides the largest gain (W-MPJPE: 1.54m \rightarrow 0.93m), with continued improvements at 3–4 views. Camera pose accuracy also benefits, with angular error reducing from 2.02° to 1.47°.

MPJPE). This advantage stems from our cross-view association module, which effectively resolves the inherent depth ambiguity in monocular estimation by aggregating complementary observations. The significant performance gap between multi-view methods and monocular Multi-HMR validates the necessity of multi-view reasoning. While optimization-based HSfM achieves lower PAMJPE through iterative pose refinement, our feed-forward approach demonstrates stronger global positioning capability without test-time optimization.

Camera Pose Estimation. As shown in Table 3, feed-forward methods demonstrate clear advantages in rotation accuracy over optimization-based approaches, likely because learned priors are more robust to local minima than iterative optimization. Notably, AHAP consistently outper-

forms the DA3 baseline across rotation and scale-aligned translation metrics, validating that human bodies serve as effective semantic landmarks providing complementary geometric constraints beyond scene features alone. While our absolute translation error is higher, the excellent scale-aligned performance indicates that the primary source of error is scale ambiguity rather than geometric misalignment—a common challenge in monocular-initialized systems that does not affect downstream human-scene consistency.

Efficiency Analysis. Unlike optimization-based approaches that necessitate costly iterative refinement, AHAP performs reconstruction in a single forward pass. Inference latency was benchmarked on an NVIDIA H200 GPU using 4-view inputs. While HSfM requires approximately 209 seconds for iterative optimization, AHAP completes the same

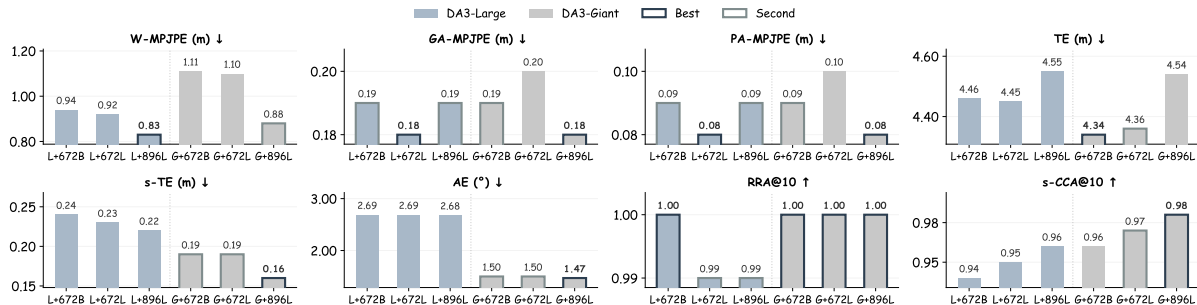


Figure 7. **Ablation study on backbone variants.** We evaluate combinations of DA3 (Large/Giant) and Multi-HMR (672B/672L/896L) backbones. Giant variants excel in camera metrics while 896L improves human reconstruction.

task in only 1.16 seconds, representing a $180\times$ speedup. Furthermore, our framework demonstrates excellent scalability, with execution time increasing only marginally from 0.89s to 1.16s when scaling from 2 to 4 views.

Qualitative Results. Visualizations in Figure 5 demonstrate that AHAP produces accurate human meshes with consistent identity association. While monocular estimations suffer from severe depth ambiguity and poor localization, our multi-view framework leverages cross-view triangulation and geometric supervision to correctly place humans in world coordinates. These mechanisms effectively enforce spatial consistency across disparate vantage points. A detailed quantitative analysis of how performance scales with the number of input views is provided in the ablation studies.

4.3. Ablation Studies

Impact of Input Views. We evaluate the sensitivity of AHAP to the number of input views during inference (Figure 6). Single-view reconstruction yields a W-MPJPE of 1.54m and a PA-MPJPE of 0.16m, reflecting inherent monocular depth ambiguities. The introduction of a second view significantly improves these metrics to 0.93m and 0.09m, respectively, before performance gains begin to plateau at 3–4 views. Regarding extrinsic calibration, translation error (TE) remains stable (4.5–4.8m), while the scale-corrected translation error (s-TE) is consistently low (≤ 0.17 m), confirming the accurate recovery of relative camera geometry. Furthermore, angular error (AE) improves steadily from 2.02° to 1.47° as additional views are incorporated. Robustness is further evidenced by registration metrics, with RRA@10 remaining at 1.00 and s-CCA@10 ≥ 0.87 across all multi-view configurations.

Backbone Variants. We evaluate the impact of different backbone scales by combining two DA3 (Lin et al., 2025) variants (Giant and Large) with three Multi-HMR (Baradel et al., 2024) variants (896L, 672L, and 672B). As shown in Figure 7, the Giant+896L configuration achieves the best overall performance. For camera pose estimation, DA3 backbone scale is the dominant factor: Giant variants consistently outperform Large variants in rotation accuracy (AE: 1.47° vs. 2.68°) and translation precision (s-TE: 0.16m vs.

Table 5. **Ablation study on key components on EgoHumans.**

Method	W-MPJPE↓	GA-MPJPE↓	PA-MPJPE↓
w/o $\mathcal{L}_{\text{reproj}}$	1.33	0.25	0.12
w/o $\mathcal{L}_{\text{assign}}$	1.33	0.24	0.11
w/o $\mathcal{L}_{\text{contra}}$	1.30	0.23	0.12
w/o $\mathcal{L}_{\text{assign}} + \text{contra}$	1.47	0.39	0.14
w/o triangulation	0.91	0.19	0.08
Full Model	0.88	0.18	0.08

0.22m), indicating that stronger geometric priors from the scene branch are essential for accurate camera recovery. For human reconstruction, Multi-HMR resolution plays a more significant role: the 896L variant yields the best W-MPJPE across both DA3 scales (0.83m for Large, 0.88m for Giant), suggesting that higher-resolution human features improve localization accuracy. We adopt Giant+896L as our default configuration to achieve the best balance between human reconstruction and camera estimation.

Key Component Ablation. We investigate the contribution of each component in Table 5. For loss functions, removing any term leads to performance degradation, confirming their synergistic roles. The reprojection loss $\mathcal{L}_{\text{reproj}}$ is the most critical; its absence results in a 51% increase in W-MPJPE (0.88m to 1.33m), as the model loses the geometric constraints necessary for cross-view consistency. The assignment loss $\mathcal{L}_{\text{assign}}$ and contrastive loss $\mathcal{L}_{\text{contra}}$ are equally vital for identity association; removing both simultaneously causes GA-MPJPE to more than double (0.18m to 0.39m). For the triangulation module, removing it leads to a modest but consistent degradation across all metrics (W-MPJPE: 0.88m to 0.91m), demonstrating that explicit 3D reasoning via triangulation provides complementary geometric cues beyond the learned features alone.

5. Conclusion

We presented AHAP, a feed-forward framework for multi-view multi-person human reconstruction from uncalibrated cameras. Our method addresses three key challenges simultaneously: cross-view identity association through learnable person queries with soft assignment, geometric consistency

via association-guided SMPL decoding, and camera-free operation by jointly estimating scene geometry and camera poses. The multi-view supervision with contrastive learning and cross-view reprojection losses enables end-to-end training with strong geometric constraints. Experiments on EgoHumans and EgoExo4D demonstrate that AHAP achieves competitive performance while being 180× faster than optimization-based methods, making it practical for real-world applications.

Impact Statements

This paper presents work whose goal is to advance the field of machine learning. There are many potential societal consequences of our work, none of which we feel must be specifically highlighted here.

References

- Agarwal, S., Furukawa, Y., Snavely, N., Simon, I., Curless, B., Seitz, S. M., and Szeliski, R. Building rome in a day. *Communications of the ACM*, 54(10):105–112, 2011.
- Baradel, F., Armando, M., Galaoui, S., Brégier, R., Weinzaepfel, P., Rogez, G., and Lucas, T. Multi-hmr: Multi-person whole-body human mesh recovery in a single shot. In *European Conference on Computer Vision*, pp. 202–218. Springer, 2024.
- Black, M. J., Patel, P., Tesch, J., and Yang, J. Bedlam: A synthetic dataset of bodies exhibiting detailed lifelike animated motion. In *Proceedings of the IEEE/CVF Conference on Computer Vision and Pattern Recognition*, pp. 8726–8737, 2023.
- Chen, C., Zhang, J., Lakshminanth, S. K., Fang, Y., Shao, R., Wetzstein, G., Fei-Fei, L., and Adeli, E. The language of motion: Unifying verbal and non-verbal language of 3d human motion. In *Proceedings of the Computer Vision and Pattern Recognition Conference*, pp. 6200–6211, 2025a.
- Chen, Y., Chen, X., Xue, Y., Chen, A., Xiu, Y., and Pons-Moll, G. Human3r: Everyone everywhere all at once. *arXiv preprint arXiv:2510.06219*, 2025b.
- Dao, A., Tran, M., Zhang, Y., Liu, X., and Cui, Z. Beyond motion pattern: An empirical study of physical forces for human motion understanding. *arXiv preprint arXiv:2512.20451*, 2025.
- Dosovitskiy, A. An image is worth 16x16 words: Transformers for image recognition at scale. *arXiv preprint arXiv:2010.11929*, 2020.
- Frahm, J.-M., Fite-Georgel, P., Gallup, D., Johnson, T., Raguram, R., Wu, C., Jen, Y.-H., Dunn, E., Clipp, B., Lazebnik, S., et al. Building rome on a cloudless day. In *European conference on computer vision*, pp. 368–381. Springer, 2010.
- Fu, H., Wang, W., Qiao, X., Yang, S., Liu, Z., and Zhao, B. Egograsp: World-space hand-object interaction estimation from egocentric videos. *arXiv preprint arXiv:2601.01050*, 2026.
- Ge, Y., Wang, W., Chen, Y., Chen, H., and Shen, C. 3d human reconstruction in the wild with synthetic data using generative models. *arXiv preprint arXiv:2403.11111*, 2024.
- Goel, S., Pavlakos, G., Rajasegaran, J., Kanazawa, A., and Malik, J. Humans in 4d: Reconstructing and tracking humans with transformers. In *Proceedings of the IEEE/CVF International Conference on Computer Vision*, pp. 14783–14794, 2023.
- Grauman, K., Westbury, A., Torresani, L., Kitani, K., Malik, J., Afouras, T., Ashutosh, K., Baiyya, V., Bansal, S., Boote, B., et al. Ego-exo4d: Understanding skilled human activity from first-and third-person perspectives. In *Proceedings of the IEEE/CVF Conference on Computer Vision and Pattern Recognition*, pp. 19383–19400, 2024.
- Huang, S., Huang, S., Luo, P., and Zhang, H. Laytrol: Preserving pretrained knowledge in layout control for multimodal diffusion transformers. *arXiv preprint arXiv:2511.07934*, 2025.
- Jaegle, A., Gimeno, F., Brock, A., Vinyals, O., Zisserman, A., and Carreira, J. Perceiver: General perception with iterative attention. In *International conference on machine learning*, pp. 4651–4664. PMLR, 2021.
- Kanazawa, A., Black, M. J., Jacobs, D. W., and Malik, J. End-to-end recovery of human shape and pose. In *Proceedings of the IEEE conference on computer vision and pattern recognition*, pp. 7122–7131, 2018.
- Khrodar, R., Bansal, A., Ma, L., Newcombe, R., Vo, M., and Kitani, K. Ego-humans: An ego-centric 3d multi-human benchmark. In *Proceedings of the IEEE/CVF International Conference on Computer Vision*, pp. 19807–19819, 2023.
- Kolotouros, N., Pavlakos, G., Black, M. J., and Daniilidis, K. Learning to reconstruct 3d human pose and shape via model-fitting in the loop. In *Proceedings of the IEEE/CVF international conference on computer vision*, pp. 2252–2261, 2019.
- Lee, J. and Yoo, S. Dense-sfm: Structure from motion with dense consistent matching. In *Proceedings of the Computer Vision and Pattern Recognition Conference*, pp. 6404–6414, 2025.

- Leroy, V., Cabon, Y., and Revaud, J. Grounding image matching in 3d with mast3r. In *European Conference on Computer Vision*, pp. 71–91. Springer, 2024.
- Li, P., Zhuang, Z., Gao, Y., Dong, Y., Li, S., Jiang, C., Dou, S., Xi, Z., Zhou, E., Huang, J., et al. From-w1: Towards general humanoid whole-body control with language instructions. *arXiv preprint arXiv:2601.12799*, 2026.
- Li, X., Meng, M., Wu, Z., Chen, T., Yang, F., and Shen, D. Human mesh recovery from arbitrary multi-view images. *arXiv preprint arXiv:2403.12434*, 2024.
- Lin, A., Zhang, J. Y., Ramanan, D., and Tulsiani, S. Rel-pose++: Recovering 6d poses from sparse-view observations. In *2024 International Conference on 3D Vision (3DV)*, pp. 106–115. IEEE, 2024.
- Lin, H., Chen, S., Liew, J., Chen, D. Y., Li, Z., Shi, G., Feng, J., and Kang, B. Depth anything 3: Recovering the visual space from any views. *arXiv preprint arXiv:2511.10647*, 2025.
- Liu, S., Gao, Y., Zhang, T., Pautrat, R., Schönberger, J. L., Larsson, V., and Pollefeys, M. Robust incremental structure-from-motion with hybrid features. In *European Conference on Computer Vision*, pp. 249–269. Springer, 2024.
- Loper, M., Mahmood, N., Romero, J., Pons-Moll, G., and Black, M. J. Smpl: A skinned multi-person linear model. In *Seminal Graphics Papers: Pushing the Boundaries, Volume 2*, pp. 851–866. ACM, 2023.
- Mildenhall, B., Srinivasan, P. P., Tancik, M., Barron, J. T., Ramamoorthi, R., and Ng, R. Nerf: Representing scenes as neural radiance fields for view synthesis. *Communications of the ACM*, 65(1):99–106, 2021.
- Müller, L., Choi, H., Zhang, A., Yi, B., Malik, J., and Kanazawa, A. Reconstructing people, places, and cameras. In *Proceedings of the Computer Vision and Pattern Recognition Conference*, pp. 21948–21958, 2025.
- Oord, A. v. d., Li, Y., and Vinyals, O. Representation learning with contrastive predictive coding. *arXiv preprint arXiv:1807.03748*, 2018.
- Pavlakos, G., Choutas, V., Ghorbani, N., Bolkart, T., Osman, A. A., Tzionas, D., and Black, M. J. Expressive body capture: 3d hands, face, and body from a single image. In *Proceedings of the IEEE/CVF conference on computer vision and pattern recognition*, pp. 10975–10985, 2019.
- Rajasegaran, J., Pavlakos, G., Kanazawa, A., and Malik, J. Tracking people by predicting 3D appearance, location & pose. In *CVPR*, 2022.
- Rojas, S., Armando, M., Ghanem, B., Weinzaepfel, P., Leroy, V., and Rogez, G. Hamst3r: Human-aware multi-view stereo 3d reconstruction. In *Proceedings of the IEEE/CVF International Conference on Computer Vision*, pp. 5027–5037, 2025.
- Salzmann, T., Chiang, H.-T. L., Ryll, M., Sadigh, D., Parada, C., and Bewley, A. Robots that can see: Leveraging human pose for trajectory prediction. *IEEE Robotics and Automation Letters*, 8(11):7090–7097, 2023.
- Schonberger, J. L. and Frahm, J.-M. Structure-from-motion revisited. In *Proceedings of the IEEE conference on computer vision and pattern recognition*, pp. 4104–4113, 2016.
- Wang, J., Rupperecht, C., and Novotny, D. Posediffusion: Solving pose estimation via diffusion-aided bundle adjustment. In *Proceedings of the IEEE/CVF International Conference on Computer Vision*, pp. 9773–9783, 2023a.
- Wang, J., Karaev, N., Rupperecht, C., and Novotny, D. Vggsfm: Visual geometry grounded deep structure from motion. In *Proceedings of the IEEE/CVF conference on computer vision and pattern recognition*, pp. 21686–21697, 2024a.
- Wang, J., Chen, M., Karaev, N., Vedaldi, A., Rupperecht, C., and Novotny, D. Vggt: Visual geometry grounded transformer. In *Proceedings of the Computer Vision and Pattern Recognition Conference*, pp. 5294–5306, 2025a.
- Wang, S., Leroy, V., Cabon, Y., Chidlovskii, B., and Revaud, J. Dust3r: Geometric 3d vision made easy. In *Proceedings of the IEEE/CVF Conference on Computer Vision and Pattern Recognition*, pp. 20697–20709, 2024b.
- Wang, W., Ge, Y., Mei, H., Cai, Z., Sun, Q., Wang, Y., Shen, C., Yang, L., and Komura, T. Zolly: Zoom focal length correctly for perspective-distorted human mesh reconstruction. In *Proceedings of the IEEE/CVF international conference on computer vision*, pp. 3925–3935, 2023b.
- Wang, W., Pan, L., Dou, Z., Mei, J., Liao, Z., Lou, Y., Wu, Y., Yang, L., Wang, J., and Komura, T. Sims: Simulating stylized human-scene interactions with retrieval-augmented script generation. In *Proceedings of the IEEE/CVF International Conference on Computer Vision*, pp. 14117–14127, 2025b.
- Wang, Y., Sun, Y., Patel, P., Daniilidis, K., Black, M. J., and Kocabas, M. Prompthmr: Promptable human mesh recovery. In *Proceedings of the Computer Vision and Pattern Recognition Conference*, pp. 1148–1159, 2025c.
- Xu, Y. and Kitani, K. Multi-view multi-person 3d pose estimation with uncalibrated camera networks. In *BMVC*, 2022.

- Ye, V., Pavlakos, G., Malik, J., and Kanazawa, A. Decoupling human and camera motion from videos in the wild. In *Proceedings of the IEEE/CVF conference on computer vision and pattern recognition*, pp. 21222–21232, 2023a.
- Ye, V., Pavlakos, G., Malik, J., and Kanazawa, A. Decoupling human and camera motion from videos in the wild. In *IEEE Conference on Computer Vision and Pattern Recognition (CVPR)*, June 2023b.
- Yin, J. O., Li, T., Wang, J., Zhang, Y., and Yuille, A. Easyret3d: Uncalibrated multi-view multi-human 3d reconstruction and tracking. In *2025 IEEE/CVF Winter Conference on Applications of Computer Vision (WACV)*, pp. 3128–3137. IEEE, 2025.
- Zhu, R., Huang, Z., Sun, J., Luo, P., Zhang, H., and Li, X. Viewmask-1-to-3: Multi-view consistent image generation via multimodal diffusion models. *arXiv preprint arXiv:2512.14099*, 2025.

A. Appendix.

B. Technical Details

B.1. SMPL Supervision Loss

We directly supervise SMPL parameters in their respective representation spaces:

$$\mathcal{L}_{\text{SMPL}} = \lambda_{\text{det}}\mathcal{L}_{\text{det}} + \lambda_{\text{param}}\mathcal{L}_{\text{param}} + \lambda_{3\text{D}}\mathcal{L}_{3\text{D}} + \lambda_{2\text{D}}\mathcal{L}_{2\text{D}}. \quad (16)$$

Detection Loss. We employ a modified focal loss This loss addresses class imbalance by down-weighting easy samples:

$$\mathcal{L}_{\text{det}} = -\frac{1}{N_{\text{pos}}} \sum_i \begin{cases} (1 - \hat{p}_i)^2 \log(\hat{p}_i) & \text{if } p_i = 1 \\ (1 - p_i)^4 \hat{p}_i^2 \log(1 - \hat{p}_i) & \text{otherwise} \end{cases}, \quad (17)$$

where p_i and \hat{p}_i denote the ground-truth and predicted scores at location i , respectively. Gaussian smoothing is applied to p_i around human centers. To achieve sub-pixel localization accuracy, we further supervise the 2D offset $\Delta \mathbf{u}$ from patch centers:

$$\mathcal{L}_{\text{offset}} = \|\Delta \hat{\mathbf{u}} - \Delta \mathbf{u}\|_1. \quad (18)$$

SMPL Parameter Loss. We directly supervise SMPL parameters in their respective representation spaces (Goel et al., 2023; Kolotouros et al., 2019):

$$\mathcal{L}_{\text{param}} = \lambda_R \|\hat{\mathbf{R}} - \mathbf{R}\|_1 + \lambda_\beta \|\hat{\boldsymbol{\beta}} - \boldsymbol{\beta}\|_1 + \lambda_d |\hat{d} - d| + \lambda_t \|\hat{\mathbf{t}} - \mathbf{t}\|_1, \quad (19)$$

where $\mathbf{R} \in \mathbb{R}^{24 \times 3 \times 3}$ represents joint $SO(3)$ to ensuress (including global orientation), supervised in $SO(3)$ to ensure gradient continuity. $\boldsymbol{\beta}$ denotes shape coefficients, while d and \mathbf{t} represent camera-space depth and 3D root translation, respectively. We utilize L_1 loss for its robustness to outliers.

3D Supervision Loss. To ensure pose and shape fidelity, we supervise root-relative 3D joints \mathbf{J} and mesh vertices \mathbf{V} :

$$\mathcal{L}_{3\text{D}} = \lambda_J \|(\hat{\mathbf{J}} - \hat{\mathbf{J}}_0) - (\mathbf{J} - \mathbf{J}_0)\|_1 + \lambda_V \|(\hat{\mathbf{V}} - \hat{\mathbf{J}}_0) - (\mathbf{V} - \mathbf{J}_0)\|_1, \quad (20)$$

where \mathbf{J}_0 is the pelvis root. This root-relative formulation decouples local body deformation from global localization, facilitating more stable learning of articulated poses.

2D Reprojection Loss. To enforce alignment with image observations, we project 3D joints and vertices onto the 2D image plane using camera intrinsics \mathbf{K} :

$$\mathcal{L}_{2\text{D}} = \lambda_{j2d} \|\Pi(\hat{\mathbf{J}}) - \mathbf{j}_{2d}\|_1 + \lambda_{v2d} \|\Pi(\hat{\mathbf{V}}) - \mathbf{v}_{2d}\|_1, \quad (21)$$

where $\Pi(\mathbf{X}) = [f_x \frac{X}{Z} + c_x, f_y \frac{Y}{Z} + c_y]^\top$. To handle occlusions, the loss is only computed for points within the image boundaries (W, H) via a validity mask:

$$\mathcal{L}_j^{2\text{D}} = \mathbf{1}[0 < j_{2d,x}^{(j)} < W] \cdot \mathbf{1}[0 < j_{2d,y}^{(j)} < H] \cdot \|\Pi(\hat{\mathbf{J}}^{(j)}) - \mathbf{j}_{2d}^{(j)}\|_1. \quad (22)$$

Training Schedule. We adopt a curriculum strategy where $\mathcal{L}_{2\text{D}}$ is enabled after 10 epochs. This allows the model to first establish a plausible 3D structure via $\mathcal{L}_{\text{param}}$ and $\mathcal{L}_{3\text{D}}$, mitigating depth ambiguities that often arise when 2D projection error dominates early training.

B.2. Implementation Details

Network Architecture. Our framework integrates two pre-trained backbones: (1) **DA3-Giant** (DINOv2-Giant) for depth and camera estimation, yielding $37 \times 37 \times 3072$ features; (2) **Multi-HMR-L** (DINOv2-Large) for mesh recovery, providing $64 \times 64 \times 1024$ features. Features are fused via a two-layer MLP ($[4096 \rightarrow 1024 \rightarrow 1024]$) with ReLU activations. The association module employs $P = 36$ learnable queries ($D = 1024$) and $H = 8$ attention heads, followed by a 2-layer Transformer decoder.

Algorithm 1 Cross-View Identity Association (Forward Pass)

Require: Multi-view detection tokens $\{\mathbf{z}_n^v\}$ for $v \in \{1, \dots, S\}$, $n \in \{1, \dots, N_v\}$; Learnable person queries $\mathbf{Q} \in \mathbb{R}^{P \times D}$;
 Reference view features $\mathbf{F}^{\text{ref}} \in \mathbb{R}^{H \times W \times D}$

Ensure: SMPL parameters $\{\theta_p, \beta_p, \mathbf{d}_p\}$ for each person p

- 1: // Stage 1: Intra-view self-attention enhancement
- 2: **for** each view $v \in \{1, \dots, S\}$ **do**
- 3: $\tilde{\mathbf{Z}}^v \leftarrow \text{LayerNorm}(\mathbf{Z}^v + \text{SelfAttn}(\mathbf{Z}^v, \mathbf{Z}^v, \mathbf{Z}^v))$
- 4: **end for**
- 5: // Stage 2: Feature projection for contrastive learning
- 6: $\mathbf{H} \leftarrow \text{LayerNorm}(\text{Proj}_{\text{contrast}}(\tilde{\mathbf{Z}}))$ ▷ $\mathbf{H} \in \mathbb{R}^{N \times D'}$, L2-normalized
- 7: // Stage 3: Cross-view soft assignment via cross-attention
- 8: $\mathbf{K} \leftarrow [\tilde{\mathbf{z}}_1, \dots, \tilde{\mathbf{z}}_N]^\top$ ▷ Concatenate all views
- 9: $\mathbf{A} \leftarrow \frac{1}{H} \sum_{h=1}^H \text{softmax} \left(\frac{\mathbf{Q} \mathbf{W}_h^Q (\mathbf{K} \mathbf{W}_h^K)^\top}{\sqrt{D/H}} \right)$ ▷ $\mathbf{A} \in \mathbb{R}^{P \times N}$
- 10: // Stage 4: Multi-view feature aggregation
- 11: **for** each person query $p \in \{1, \dots, P\}$ **do**
- 12: $\mathbf{f}_p^{\text{agg}} \leftarrow \text{LayerNorm}(\mathbf{A}_{p,:} \cdot \mathbf{K})$ ▷ Weighted sum
- 13: **end for**
- 14: // Stage 5: Person-to-detection assignment
- 15: **for** each detection n **do**
- 16: $\text{person}(n) \leftarrow \arg \max_p \mathbf{A}_{p,n}$
- 17: **end for**
- 18: // Stage 6: Multi-view context injection into Human Head
- 19: **for** each person p with assigned detections **do**
- 20: $\tilde{\mathbf{C}} \leftarrow \mathbf{C}^{\text{ref}} + \sigma(\alpha) \cdot \text{Broadcast}(\text{Proj}_{\text{kv}}(\mathbf{f}_p^{\text{agg}}))$ ▷ Context injection
- 21: $\mathbf{q}_{\text{mv}} \leftarrow \text{Proj}_{\text{q}}(\mathbf{f}_p^{\text{agg}})$ ▷ Query injection
- 22: $\mathbf{q}_{\text{det}} \leftarrow [\mathbf{z}_{\text{ref}}; \boldsymbol{\theta}; \boldsymbol{\beta}; \tilde{\mathbf{c}}]$
- 23: $\mathbf{q}_{\text{final}} \leftarrow \text{CrossAttn}([\mathbf{q}_{\text{det}}; \mathbf{q}_{\text{mv}}], \tilde{\mathbf{C}}, \tilde{\mathbf{C}})$
- 24: $\theta_p, \beta_p, \mathbf{d}_p \leftarrow \text{MLP}_{\text{pose/shape/cam}}(\mathbf{q}_{\text{final}})$
- 25: **end for**
- 26: **return** $\{\theta_p, \beta_p, \mathbf{d}_p, \mathbf{A}, \mathbf{H}\}$

Two-Stage Training. *Stage 1:* Pre-training on BEDLAM synthetic sequences (4 consecutive frames as pseudo-multi-view) for 50 epochs. We use AdamW with an effective batch size of 32. The learning rate follows a linear warmup (10^{-8} to 10^{-4}) followed by cosine decay. *Stage 2:* Fine-tuning on real multi-view EgoHumans data (2-4 synchronized views) for 50 epochs. We introduce cross-view reprojection losses ($\lambda_{\text{crossview.j3d}} = 10.0$, $\lambda_{\text{crossview.j2d}} = 1.0$) and increase weight decay to 0.01. Throughout both stages, backbones remain frozen while task-specific heads and fusion modules are optimized. All experiments are conducted on $4 \times$ NVIDIA H200 GPUs with distributed training.

Loss Weights. For detection losses, we use $\lambda_{\text{bce}} = 0.01$ and $\lambda_{\text{offset}} = 1.0$. For SMPL parameter supervision, we set $\lambda_{\text{rotmat}} = 0.1$, $\lambda_{\text{shape}} = 1.0$, $\lambda_{\text{dist}} = 1.0$, and $\lambda_{\text{transl}} = 1.0$. The 3D supervision losses use $\lambda_{\text{j3d}} = 100.0$ and $\lambda_{\text{v3d}} = 100.0$, while the 2D reprojection losses use $\lambda_{\text{j2d}} = 1.0$ and $\lambda_{\text{v2d}} = 1.0$. For association losses, we set $\lambda_{\text{assign}} = 1.0$ and $\lambda_{\text{contra}} = 1.0$. In Stage 2, we additionally apply cross-view reprojection losses with $\lambda_{\text{crossview.j3d}} = 10.0$ and $\lambda_{\text{crossview.j2d}} = 1.0$.

Cross-View Identity Association Algorithm. We provide the complete algorithmic description of our Cross-View Identity Association module. Algorithm 1 describes the forward pass, which proceeds in six stages: (1) intra-view self-attention enhances each detection’s representation by considering other people in the same view; (2) feature projection maps tokens to a normalized embedding space for contrastive learning; (3) cross-attention between learnable person queries and all detection tokens produces a soft assignment matrix; (4) weighted aggregation pools multi-view information per person; (5) greedy assignment maps detections to person identities; and (6) the Human Head receives aggregated features via both context injection (enhancing key-value features) and query injection (auxiliary attention token).

Dynamic Query Selection. Although we initialize $P = 36$ learnable person queries to accommodate scenes with many individuals, the actual number of queries used during inference adapts to scene complexity. Specifically, we compute

$P_{\text{active}} = \min(\max_v N_v, P)$, where N_v denotes the number of detected humans in view v . Only the first P_{active} queries participate in cross-attention, reducing computational overhead for sparse scenes. Furthermore, after soft assignment, queries that receive no detection assignments (i.e., $\sum_n \mathbf{A}_{p,n} < \epsilon$ for all detections) are filtered out, ensuring that only queries corresponding to actual persons proceed to the Human Head for SMPL regression. This dynamic mechanism enables efficient handling of scenes ranging from single-person to crowded multi-person scenarios without architectural changes.

Dynamic Query Selection. Although we initialize $P = 36$ learnable person queries to accommodate scenes with many individuals, the actual number of queries used during inference adapts to scene complexity. Specifically, we compute $P_{\text{active}} = \min(\max_v N_v, P)$, where N_v denotes the number of detected humans in view v . Only the first P_{active} queries participate in cross-attention, reducing computational overhead for sparse scenes. Furthermore, after soft assignment, queries that receive no detection assignments (i.e., $\sum_n \mathbf{A}_{p,n} < \epsilon$ for all detections) are filtered out, ensuring that only queries corresponding to actual persons proceed to the Human Head for SMPL regression. This dynamic mechanism enables efficient handling of scenes ranging from single-person to crowded multi-person scenarios without architectural changes.

Cross-View Association Loss. Algorithm 2 describes the loss computation, which combines three complementary objectives: (1) **soft assignment loss** directly supervises attention weights using Hungarian matching to align predicted and GT person identities, followed by cross-entropy; (2) **InfoNCE contrastive loss** pulls together features of the same person across different views while pushing apart different individuals; and (3) **cross-view reprojection loss** enforces geometric consistency by transforming predictions from the reference view to other views and comparing with GT in both 3D (root-relative) and 2D (projected) spaces.

B.3. Data Augmentation

Maintaining geometric consistency across views and modalities (depth, camera, SMPL) is critical. Our augmentation pipeline is designed to preserve these relationships under transformation.

Geometric Augmentations. We apply random rotation ($\pm 30^\circ$) and scaling ($[0.8, 1.2]$). For each rotation, we update camera extrinsics and transform SMPL global orientation/translation via forward kinematics to maintain camera-world alignment. Camera intrinsics are scaled proportionally to scaling factors. For cropping, we use the union bounding box of all humans with a 5% random translation. Non-square crops are zero-padded to square before resizing to 896×896 .

Photometric Augmentations. We apply color jittering (brightness/contrast/saturation ± 0.5 , hue ± 0.1) with 0.9 probability and grayscale conversion with 0.05 probability. In Stage 2, we use a *co-jittering* strategy (ratio 0.3) to balance cross-view consistency with individual view diversity.

Annotation Consistency. Post-augmentation, the principal point is re-centered to $(W/2, H/2)$ for a canonical camera model. While body-local pose and shape remain invariant, global orientation is transformed by the inverse rotation matrix around the Z-axis, and root translation is updated accordingly to ensure the projected mesh remains aligned with the augmented image.

C. Experimental Details

C.1. Evaluation Details

We employ the following metrics to evaluate human pose estimation and camera localization. To ensure fair comparison, predicted results are aligned with ground truth via $SE(3)$ (rigid) or $Sim(3)$ (similarity) transformations as specified.

C.1.1. HUMAN POSE METRICS

W-MPJPE (World Mean Per-Joint Position Error) measures the average Euclidean distance between predicted and ground-truth 3D joint positions in the world coordinate frame, after $SE(3)$ alignment of predicted camera trajectories to ground truth.

PA-MPJPE (Procrustes-Aligned MPJPE) computes the joint position error after per-person $Sim(3)$ alignment, which removes global translation, rotation, and scale. This metric evaluates local pose accuracy independent of camera estimation or body scale.

GA-MPJPE (Group-Aligned MPJPE) applies a single $Sim(3)$ alignment to all humans in a scene simultaneously, measuring their relative spatial configurations without considering absolute world positioning.

Algorithm 2 Cross-View Association Loss Computation

Require: Soft assignment $\mathbf{A} \in \mathbb{R}^{P \times N}$; Projected features $\mathbf{H} \in \mathbb{R}^{N \times D'}$; Predicted joints $\{\mathbf{J}_p^{\text{ref}}\}$; GT correspondences $\{(p^*, \{(v, n)\})\}$; Camera extrinsics $\{\mathbf{C2W}^v, \mathbf{W2C}^v\}$

Ensure: Total association loss $\mathcal{L}_{\text{assoc}}$

```

1: // Loss 1: Soft Assignment Supervision
2:  $\mathbf{A}^* \leftarrow \mathbf{0}^{P^* \times N}$  ▷ Construct GT assignment matrix
3: for each GT person  $p^*$  with detections  $\{(v_i, n_i)\}$  do
4:   for each  $(v_i, n_i)$  do
5:      $\mathbf{A}_{p^*, \text{global}(v_i, n_i)}^* \leftarrow 1$ 
6:   end for
7:    $\mathbf{A}_{p^*, :}^* \leftarrow \mathbf{A}_{p^*, :}^* / \|\mathbf{A}_{p^*, :}^*\|_1$  ▷ Row normalization
8: end for
9:  $\pi \leftarrow \text{HungarianMatch}(\mathbf{A}, \mathbf{A}^*)$  ▷ Optimal assignment
10:  $\mathcal{L}_{\text{assign}} \leftarrow -\frac{1}{P^*} \sum_{p^*} \sum_n \mathbf{A}_{p^*, n}^* \log \mathbf{A}_{\pi(p^*), n}$ 
11: // Loss 2: InfoNCE Contrastive Learning
12:  $\mathcal{P} \leftarrow \emptyset$  ▷ Positive pairs: same person, different views
13: for each GT person  $p^*$  with detections in  $\geq 2$  views do
14:   for each pair  $(n_i, n_j)$  where  $v_i \neq v_j$  do
15:      $\mathcal{P} \leftarrow \mathcal{P} \cup \{(n_i, n_j)\}$ 
16:   end for
17: end for
18:  $\mathcal{L}_{\text{contra}} \leftarrow -\frac{1}{|\mathcal{P}|} \sum_{(i, j) \in \mathcal{P}} \log \frac{\exp(\mathbf{h}_i \cdot \mathbf{h}_j / \tau)}{\sum_{k \neq i} \exp(\mathbf{h}_i \cdot \mathbf{h}_k / \tau)}$ 
19: // Loss 3: Cross-View Geometric Consistency
20:  $\mathcal{L}_{\text{reproj}} \leftarrow 0$ 
21: for each person  $p$  visible in reference view do
22:    $\mathbf{J}_{\text{world}} \leftarrow \mathbf{C2W}^{\text{ref}} \cdot \mathbf{J}_p^{\text{ref}}$  ▷ Transform to world
23:   for each other view  $v$  where person  $p$  is visible do
24:      $\mathbf{J}_{\text{pred}}^v \leftarrow \mathbf{W2C}^v \cdot \mathbf{J}_{\text{world}}$  ▷ Project to view  $v$ 
25:      $\mathbf{J}_{\text{gt}}^v \leftarrow \text{GT joints in view } v$ 
26:      $\mathcal{L}_{\text{reproj}} += \|(\mathbf{J}_{\text{pred}}^v - \mathbf{J}_{\text{pred}, 0}^v) - (\mathbf{J}_{\text{gt}}^v - \mathbf{J}_{\text{gt}, 0}^v)\|_1$  ▷ Root-relative 3D
27:      $\mathcal{L}_{\text{reproj}} += \lambda_{2d} \|\Pi(\mathbf{J}_{\text{pred}}^v) - \mathbf{j}_{\text{gt}}^{v, 2d}\|_1$  ▷ 2D reprojection
28:   end for
29: end for
30: // Total Association Loss
31:  $\mathcal{L}_{\text{assoc}} \leftarrow \lambda_1 \mathcal{L}_{\text{assign}} + \lambda_2 \mathcal{L}_{\text{contra}} + \lambda_3 \mathcal{L}_{\text{reproj}}$ 
32: return  $\mathcal{L}_{\text{assoc}}$ 

```

C.1.2. CAMERA LOCALIZATION METRICS

TE (Translation Error) measures the mean Euclidean distance between predicted and ground-truth camera centers after $SE(3)$ alignment, evaluating metric accuracy of camera positions.

s-TE (Scale-aligned TE) is computed after $Sim(3)$ alignment, providing scale-invariant evaluation of camera position estimates.

AE (Angular Error) measures the average angular discrepancy (in degrees) between predicted and ground-truth pairwise camera orientations across the scene.

CCA@ τ (Camera Center Accuracy) measures the proportion of cameras localized within $\tau\%$ of the overall scene scale after $SE(3)$ alignment. **s-CCA@ τ** denotes the scale-aligned version using $Sim(3)$.

RRA@ τ (Relative Rotation Accuracy) measures the percentage of camera pairs with relative rotation error within τ degrees.

C.1.3. EVALUATION DATASETS

EgoHumans. We evaluate on the following sequences from EgoHumans. Table 6 summarizes the evaluation sequences and camera configurations.

Table 6. EgoHumans evaluation sequences and camera configurations.

Activity	Sequences	Cameras
01_tagging	001-014	1, 4, 6, 8
02_lego	001-006	2, 3, 4, 6
03_fencing	001-014	4, 5, 10, 13
04_basketball	001-014	1, 3, 4, 8
05_volleyball	001-011	2, 4, 8, 11
06_badminton	001-061	1, 2, 5, 7
07_tennis	001-013	4, 9, 12, 20

EgoExo4D. EgoExo4D scenes are typically captured using four to six RGB cameras and an egocentric device (Aria glasses). For our experiments and the baselines, we use only the RGB images from sequences with correct re-identification. Sequences containing ego-centric RGB views, such as helmet-mounted cameras, are excluded. We evaluate 182 videos from the validation set, sampling one random frame per video. The videos include ground-truth annotations for human poses, locations, and camera parameters.

Note that EgoExo4D uses COCO 17 keypoints, while our model outputs SMPL 24 joints. We evaluate on the common joints between them: shoulders, elbows, wrists, hips, knees, and ankles (12 joints total).

Table 7 lists all evaluation takes and frame indices.

C.2. Training Data Statistics

BEDLAM (Stage 1). To establish a robust foundation, we utilize 21 synthetic scenes from the BEDLAM dataset, encompassing diverse indoor and outdoor environments such as offices, gyms, and suburbs. Each scene contains 250–1000 frames with 3–10 subjects per i-view constraints by sampling 4 consecutive temporal frames per training instance. Following the official protocol, we divide the dataset into training and validation sets, comprising 75% and 20% of the total 1M unique bounding boxes, respectively.

EgoHumans (Stage 2). For Stage 2 training, we use sequences that are disjoint from the evaluation set. Specifically, we train on basketball (13 sequences), volleyball (11 sequences), badminton (61 sequences), and tennis (13 sequences) activities, while the evaluation is performed on tagging (14 sequences), lego assembly (6 sequences), and fencing (14 sequences) activities. This ensures zero overlap between training and evaluation data, allowing us to assess generalization to unseen activities and scenes. Each sequence is captured by 4–8 synchronized cameras, and we randomly sample 2–4 camera views per training sample.

C.3. Additional Ablation Results

Table 8 provides the complete numerical results for the backbone ablation study visualized in the main paper. We evaluate different combinations of DA3 backbone sizes (Large, Giant) and Multi-HMR configurations (input resolution and backbone size). The Giant DA3 backbone with 896×896 Multi-HMR-Large (896 L) achieves the best overall performance, balancing human pose accuracy and camera localization metrics.

Table 9 provides the complete numerical results for the number of views ablation study visualized in the main paper. We evaluate the impact of increasing the number of input views from 1 to 4. With a single view, only human pose metrics are available. As the number of views increases, both human pose accuracy and camera localization improve, with 4 views achieving the best overall performance.

C.4. Additional Qualitative Results

We provide additional qualitative results to demonstrate the effectiveness of our method across diverse scenarios. Figure 8 shows multi-person reconstruction with accurate pose estimation and camera localization. Figure 9 demonstrates robustness in cluttered environments with varying viewpoints.

Submission and Formatting Instructions for ICML 2026

Table 7. EgoExo4D evaluation takes and frame indices.

Dataset	Takes / Frame Indices	Dataset	Takes / Frame Indices
cmu_soccer	06_3/1426, 12_2/6807, 16_2/6373	unc_basketball	02-24-23_01_3/84, 02-24-23_02_10/466, 02-24-23_02_11/927, 03-30-23_02_10/45, 03-30-23_02_14/7, 03-30-23_02_15/40, 03-30-23_02_17/9, 03-30-23_02_18/20, 03-30-23_02_19/7, 03-30-23_02_4/107, 03-30-23_02_5/25, 03-30-23_02_7/1141
georgiatech_bike	06_12/170, 06_2/97, 06_6/74, 06_8/15, 07_10/28, 07_12/38, 07_2/97, 07_4/46, 07_6/67, 07_8/138, 14_12/593, 14_2/1214, 14_6/575, 14_8/97, 15_2/1508, 15_4/844, 15_6/1103, 15_8/3153, 16_2/882, 16_6/3031, 16_8/1274	uniandes_basketball	001_23/768, 001_24/1386, 001_26/146, 001_27/439, 003_38/32, 004_23/369, 004_44/261, 004_45/667
georgiatech_covid	02_10/2227, 02_12/6974, 02_14/2926, 02_2/67, 02_4/67, 04_10/999, 04_12/6160, 04_4/2996, 04_6/4528, 06_2/47, 06_4/64, 18_10/5524, 18_12/3457, 18_2/2413, 18_4/3534, 18_6/4389, 18_8/458	uniandes_dance	002_11/201, 002_2/439, 008_29/276, 008_30/166, 008_31/31, 008_32/11, 008_33/1105, 008_34/753, 008_35/607, 008_36/1045, 008_37/913, 008_38/706, 016_10/841, 016_11/279, 016_12/932, 016_13/453, 016_14/951, 016_30/577, 016_31/1709, 016_32/377, 016_33/1158, 016_36/1247, 016_37/145, 016_38/1416, 016_39/399, 016_3/1239, 016_42/1406, 016_43/1271, 016_44/1268, 016_45/838, 016_6/1361, 016_7/1040, 016_8/1488, 017_6/1592, 019_17/1003, 019_18/509, 019_19/1537, 019_20/1089, 019_22/81, 019_24/484, 019_25/183, 019_26/1814, 019_27/283, 019_28/1411, 019_46/412, 019_47/790, 019_49/1617, 019_51/481, 019_52/875, 019_54/766, 019_55/679, 019_56/561, 019_57/1073, 019_58/192, 024_11/1619, 024_12/104, 024_13/1419, 024_14/1180, 024_15/378, 024_16/1569, 024_17/1317, 024_45/844, 024_47/732, 024_48/261, 024_49/325
iiith_cooking	59_2/7795, 64_2/298, 89_6/1177, 90_4/1383	upenn_Dance	0706_4_2/2512, 0706_4_3/1277, 0706_4_4/1670, 0706_4_5/1904, 0713_3_2/164, 0713_3_3/586, 0713_3_4/0, 0713_3_5/243, 0713_4_2/125, 0713_4_3/1280, 0713_4_4/308, 0713_4_5/262, 0713_5_4/238, 0713_5_6/2534
iiith_soccer	015_2/1610	upenn_Piano	0721_1_2/140, 0721_1_3/648, 0722_1_2/83, 0727_Partner_Dance_3_1_2/62
nus_cpr	12_1/1338, 12_2/76	utokyo_per	2001_29_2/5799, 2001_29_4/3491, 2001_29_6/550, 2001_30_2/2121, 2001_30_4/1696, 2001_32_2/6641, 2001_32_4/6048
sfu_basketball	012_10/774, 012_12/399, 012_2/945, 012_3/1506, 012_4/66, 012_6/526, 012_7/1581, 012_8/329, 016_2/247, 04_8/209, 05_22/1902, 05_26/29, 09_11/32, 09_12/1114	utokyo_soccer	8000_43_2/3262, 8000_43_4/3472, 8000_43_6/2781
sfu_cooking	028_12/1049, 007_7/77, 008_3/4164, 008_5/3559		
sfu_covid	004_2/2828, 004_4/5360, 008_16/1595		

C.5. Failure Cases

We also present failure cases of our method. As shown in Figure 10, the reconstructed humans appear floating above the ground.

Table 8. Ablation study on backbone variants on EgoHumans. Best and second best results are highlighted.

DA3	Multi-HMR	Human Metrics			Camera Metrics				
		W-MPJPE↓	GA-MPJPE↓	PA-MPJPE↓	TE↓	s-TE↓	AE↓	RRA@10↑	s-CCA@10↑
Large	672_B	0.94	<u>0.19</u>	<u>0.09</u>	4.46	0.24	2.69	1.00	0.94
Large	672_L	0.92	0.18	0.08	4.45	0.23	2.69	<u>0.99</u>	0.95
Large	896_L	0.83	<u>0.19</u>	<u>0.09</u>	4.55	0.22	2.68	<u>0.99</u>	0.96
Giant	672_B	1.11	<u>0.19</u>	<u>0.09</u>	4.34	<u>0.19</u>	<u>1.50</u>	1.00	0.96
Giant	672_L	1.10	0.20	0.10	<u>4.36</u>	<u>0.19</u>	<u>1.50</u>	1.00	<u>0.97</u>
Giant	896_L	<u>0.88</u>	0.18	0.08	4.54	0.16	1.47	1.00	0.98

Table 9. Ablation study on the number of views on EgoHumans. Best and second best results are highlighted.

Num. Views	Human Metrics			Camera Metrics				
	W-MPJPE↓	GA-MPJPE↓	PA-MPJPE↓	TE↓	s-TE↓	AE↓	RRA@10↑	s-CCA@10↑
1	1.54	0.16	0.16	-	-	-	-	-
2	0.93	0.25	<u>0.09</u>	<u>4.72</u>	<u>0.17</u>	2.02	1.00	1.00
3	<u>0.90</u>	0.23	0.08	4.79	<u>0.17</u>	<u>1.63</u>	1.00	0.87
4	0.88	<u>0.18</u>	0.08	4.54	0.16	1.47	1.00	<u>0.98</u>

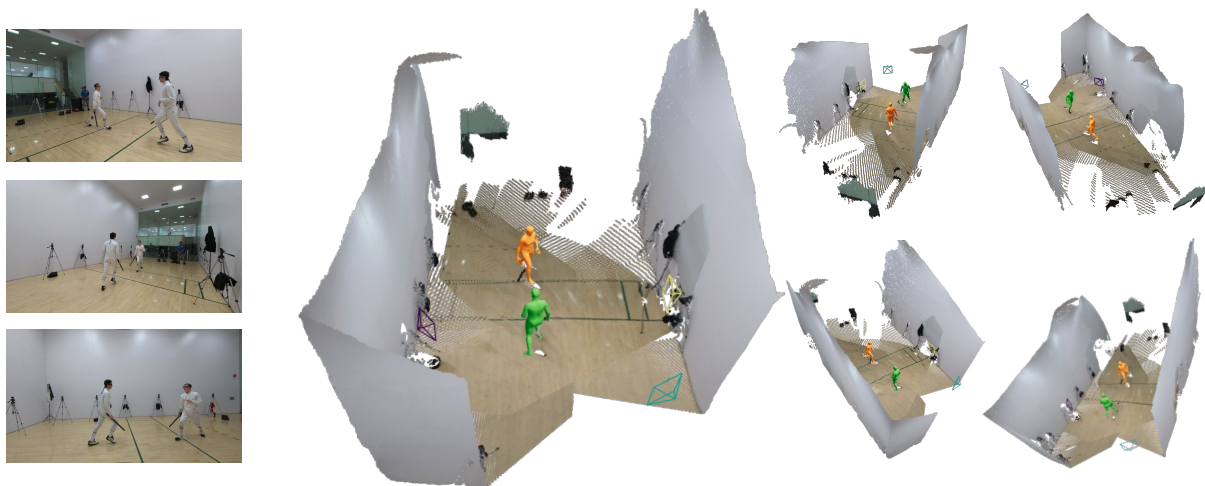


Figure 8. Additional qualitative results. Our method accurately reconstructs the 3D poses of two individuals (shown in orange and green) and recovers the camera poses from five different viewpoints. The scene point cloud and camera frustums are visualized together with the SMPL meshes, demonstrating consistent multi-view reconstruction.

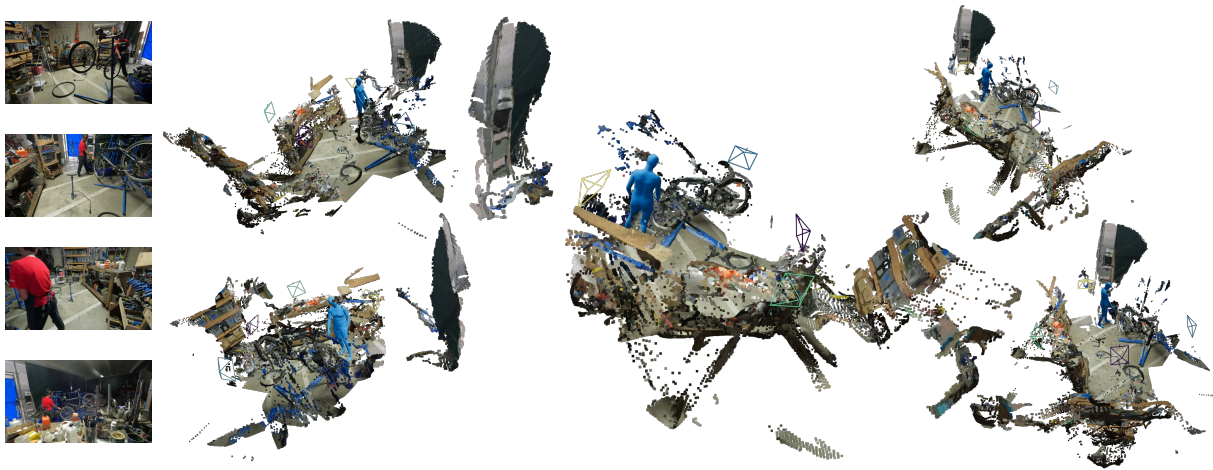


Figure 9. **Additional qualitative results.** Our method successfully handles complex real-world scenarios with cluttered backgrounds, diverse objects, and varying camera viewpoints. The reconstructed human (shown in blue) is accurately localized across 5 different camera views, demonstrating robustness to challenging scene conditions.



Figure 10. **Failure case.** The reconstructed human meshes appear floating above the ground plane, with feet not properly aligned with the floor surface.